Measuring shock-bang timing and ρR evolution of D^3He implosions at OMEGA[a)]

J. A. Frenje,[b)] C. K. Li, F. H. Séguin, J. Deciantis, S. Kurebayashi, J. R. Rygg, and R. D. Petrasso[c)]
Plasma Science and Fusion Center, Massachusetts Institute of Technology, Cambridge, Massachusetts 02139

J. Delettrez, V. Yu. Glebov, C. Stoeckl, F. J. Marshall, D. D. Meyerhofer,[d)] T. C. Sangster, V. A. Smalyuk, and J. M. Soures
Laboratory for Laser Energetics, University of Rochester, Rochester, New York 14623

(Received 30 October 2003; accepted 12 February 2004; published online 23 April 2004)

New experimental results describing the dynamics of D^3He capsule implosions, performed at the 60 beam direct-drive OMEGA laser system [T. R. Boehly *et al.*, Opt. Commun. **133**, 495 (1997)], are presented. The capsules, nominally 940 μm in diameter and with 20–27 μm thick CH shells, were filled with 18 atm D^3He gas and irradiated with 23 kJ of UV light. Simultaneous measurements of D^3He burn history, DD burn history, and several time-integrated D^3He proton energy spectra provided new results, such as shock-bang timing, shock-burn duration, evolution of the ion temperature, and evolution of ρR and ρR asymmetries. The shock-bang time measurements, when compared to calculation using the 1D LILAC code [J. Delettrez *et al.*, Phys. Rev. A **36**, 3926 (1987)], indicate that a varying flux limiter is required to explain the data, while the measured shock-burn duration is significantly shorter than 1D calculations, irrespective of flux limiter. The time evolution of ion temperature $[T_i(t)]$ has been inferred from the ratio of the DD and the D^3He burn histories, and a constant temperature is observed during the compression phase. The discrepancy between experimental data and 1D simulations during the final stages of the compression burn indicates that mix is significant, especially for the 20 and 24-μm capsule implosions. Evolution of ρR and ρR asymmetries show that the average ρR grows by a factor of $\sim 4-5$ from shock-bang to compression-bang time, and that ρR asymmetries ($l=1$), primarily driven by capsule convergence, grows ~ 2 times faster than the average ρR growth. © *2004 American Institute of Physics.* [DOI: 10.1063/1.1695359]

I. INTRODUCTION

Shock convergence timing and proper assembly of capsule mass, as manifested through areal density (ρR) evolution, are fundamentally important for achieving ignition in inertial confinement fusion (ICF).[1–3] Experimental information about implosion dynamics is therefore required both for understanding how assembly occurs and for critically evaluating numerical simulations. Without carefully tailored assembly of the fuel, hot-spot ignition planned for the National Ignition Facility (NIF) (Refs. 1–4) and the Laser Mega Joule (LMJ) facility[5] will fail. Hot spot ignition relies on shock convergence to ''ignite'' the hot spot, followed by propagation and burn of the compressed shell material (compressive burn). The relationship between these events must be understood to ensure the success of ICF ignition. To elucidate these issues, we report here the first precise measurements of shock-bang timing, shock-burn duration, and evolution of the ion temperature of D^3He implosions. These measurements were performed at the 60 beam direct-drive OMEGA laser system.[6] For the shock-bang timing studies, the unique strength of the D^3He shock burn and its clear separation from the compression burn, as opposed to other nuclear reactions (DD or DT), allow highly accurate timing measurements. In addition, data describing evolution of ρR and ρR asymmetries of these types of implosions are reported.

Inferring ρR is accomplished by studying the slowing down of the energetic D^3He protons. Through the use of plasma stopping power calculations,[7] these energy downshifts are quantitatively related to the ρR of the plasma material. Although most ρR and ρR asymmetry studies, utilizing the energetic D^3He protons, have been time-integrated studies over the entire D^3He burn,[8–15] D^3He proton spectra often show unique signatures of ρR evolution. In particular, Ref. 12 clearly demonstrates that measured D^3He proton spectra have two distinctive features associated with shock and compression phases of the implosion. Furthermore, it was suggested in Ref. 13, that ρR asymmetries at compression-bang time, relative to the ρR asymmetries at shock-bang time, have been amplified without any phase changes; an effect that was demonstrated later in Ref. 14 for capsules imploded using a large imposed laser-drive asymmetry. In addition, the work described in Ref. 16 combines time-integrated D^3He proton spectra with measured DD burn history to infer ρR evolution during the DD burn. That work, however, did not evaluate ρR asymmetries, and was only

[a)]Paper FI2 4, Bull. Am. Phys. Soc. **48**, 86 (2003).
[b)]Invited speaker.
[c)]Also Visiting Senior Scientist at LLE.
[d)]Also at Department of Mechanical Engineering, Physics and Astronomy.

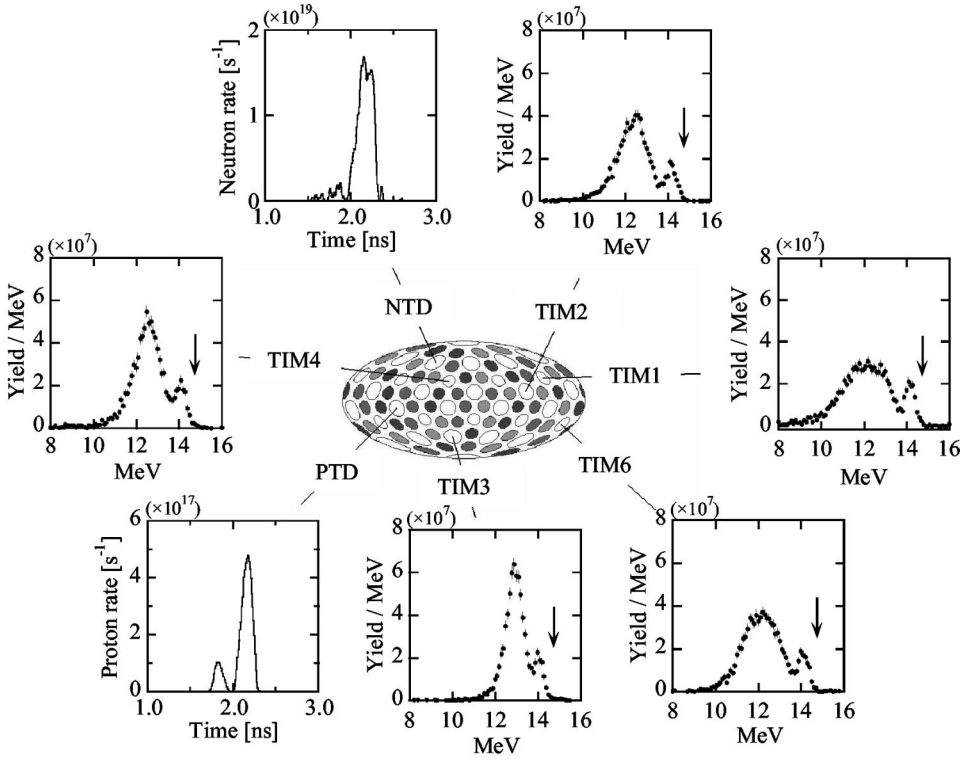

FIG. 1. Schematic drawing of the OMEGA target chamber showing the position of the neutron temporal diagnostic (NTD), and the locations of ports TIM 1 through TIM 6 that were used for the proton spectrometers and for the proton temporal diagnostic (PTD). Also shown is a corresponding set of measured D^3He proton spectra, NTD, and PTD data from a D^3He implosion with a 27-μm thick CH shell (shot 31271). The energy down shift of the spectrum is a direct measure of ρR along the line-of-sight of each spectrometer (the birth energy of the D^3He protons is 14.7 MeV as indicated by the arrows in the spectra). The narrow high-energy peak is associated with the shock burn, and the wider low-energy peak with the compressive burn.

applied to capsule implosions when the D^3He-shock yield was insignificant in comparison to the compression yield.

The work described herein extends aspects of the work described in Refs. 12–16 by combining D^3He burn history data with time-integrated D^3He proton spectra measured simultaneously from several directions. This allows highly accurate studies of the nature of D^3He burn from which studies of shock-bang timing and duration, evolution of ion temperature, evolution of ρR and ρR asymmetries for many types of implosions. This paper is structured as follows: Sec. II describes the experiments, while Sec. III describes the data processing and analysis. In Sec. IV, the results are discussed and contrasted to 1D calculations, while Sec. V gives a few remarks on planned future activities. Finally, Sec. VI concludes the paper.

II. EXPERIMENTS

In these experiments, capsules were imploded with a 1-ns square laser pulse shape delivering about 23 kJ of UV-energy on target. All laser beams on OMEGA were smoothed with SG3 distributed phase plates,[17] 1-THz, two-dimensional smoothing by spectral dispersion,[18] and polarization smoothing using birefringement wedges;[19] the beam-to-beam energy imbalance was typically 3%–4% rms for these implosions. D^3He filled CH capsules with a nominal diameter of 940 μm, a nominal fill pressure of 18 atm, and shell thickness varying from 20 to 27 μm were used. These implosions were studied using a proton temporal diagnostic (PTD) for measurement of D^3He burn history,[20] and several proton spectrometers for measurements of time-integrated D^3He proton energy spectra. Additional information about the implosions was obtained from the neutron temporal diagnostic (NTD) (Refs. 21, 22) that measures the DD burn history as described in Sec. III. The primary reactions utilized in these experiments are

$$D + {}^3He \rightarrow {}^4He(3.6\ \text{MeV}) + p(14.7\ \text{MeV}), \quad (1)$$

$$D + D \rightarrow {}^3He(0.82\ \text{MeV}) + n(2.45\ \text{MeV}). \quad (2)$$

Up to six proton spectrometers, which are described in detail in Ref. 9, were simultaneously used for the time-integrated measurements of the D^3He proton spectrum. The spectrometers were used in the OMEGA target chamber diagnostic ports TIM1 through TIM4 and TIM6 as shown in Fig. 1. This figure also shows the port locations that were used for the PTD (TIM5) and the NTD, as well as a set of measured D^3He proton spectra from a D^3He implosion with a 27-μm thick CH shell (shot 31271).

The PTD consists of a 1-mm thick BC422 scintillator and a thin (about 100 μm) tantalum filter in front of the scintillator for protection against x rays and laser light. An optical system transports the scintillator light produced by the D^3He protons in the scintillator to a high-speed optical streak camera,[23] located outside the target chamber. The BC422 scintillator is positioned 9 cm from the implosion. A train of optical fiducial signals is simultaneously recorded for an accurate timing reference with respect to the laser pulse. A drawing of the PTD front end is shown in Fig. 2(a). Figure 2(b) shows a streaked image recorded by a CCD camera attached to the streak camera for shot 31271. The horizontal axis corresponds to time, and the train of optical fiducial signals is shown just above the image of the scintillator output. The vertical direction reflects the image of the scintillator, and the measured signal is averaged across this direction after the signal has been corrected for background (measured

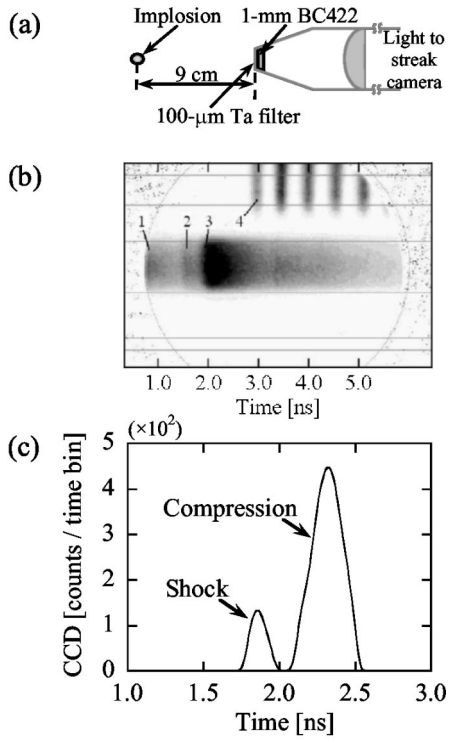

FIG. 2. (a) Schematic drawing of the PTD front end that is positioned 9 cm from the implosion, (b) streaked image recorded by a CCD camera attached to a streak camera, and (c) resulting time history of deconvolved D^3He burn, which indicates both shock burn and compression burn for shot 31271. The PTD front end, shown in (a), consists of a 1 mm thick BC422 scintillator and a thin (about 100 μm) tantalum filter in front of the scintillator for protection against x rays and laser light. A train of optical fiducial signals (labeled 4), which is shown just above the image of the scintillator output, is used for the timing reference. Also indicated in the image is the x-ray component (labeled 1), shock component (labeled 2), and compression component (labeled 3). The vertical direction indicates the image of the scintillator, and the background corrected signal is averaged across this direction. The resulting time history of the deconvolved signal, as shown in (c), is in turn a convolution of real D^3He burn history, arrival time spread at the PTD caused by several effects as described in Sec. III, and PTD response. Post processing of the deconvolved PTD signal must therefore be performed to determine the real D^3He burn history [see Fig. 4(b)].

in the bottom portion of the image), geometric distortions, and the streak camera flat field. Due to the very fast scintillator risetime (<20 ps) and the slow decay time (~ 1.2 ns), the burn history is encoded in the leading edge of the measured signal. The resulting D^3He burn history (the deconvolved signal), shown in Fig. 2(c), is therefore obtained by deconvolving the effect of the long scintillator decay time from the recorded signal. To obtain the absolute timing of the deconvolved signal, all protons were assumed to have the energy of 14.3 MeV. The resulting time history of the signal, shown in Fig. 2(c), is in turn a convolution of real D^3He burn history, arrival time spread at the PTD caused by several effects as described in Sec. III, and PTD response. The actual proton energy spectra shown in Fig. 1 were used in the subsequent post processing of the deconvolved D^3He burn history as described in the next section.

III. DATA PROCESSING AND ANALYSIS

To determine time evolution of the D^3He burn from the deconvolved PTD signal that is shown in Fig. 2(c), the data must be corrected for the effects causing time dispersion at the PTD. These effects are: Doppler broadening, geometric broadening, ρR evolution, and PTD response. In this context, the PTD position relative to the implosion has to be considered as well. Basically, the energy spectrum of emitted D^3He protons, born at a particular time t has been broadened due to ion temperature and implosion geometry and downshifted in energy due to ρR (primarily due to the shell at all times). As a result of the spectral broadening, these D^3He protons will arrive at the PTD at different times. Additional spectral broadening, and the resulting time dispersion, is introduced as ρR evolves in time, $[\rho R(t)]$, which is also one of the most important physical quantities to characterize (Sec. IV C). Temporal broadening is also caused by PTD response. The significance and effects of each process are described in detail in the next section.

A. Components causing time spread in PTD data

Although Doppler broadening caused by ~ 6 keV ion temperature (T_i) (Ref. 12) dominates other effects at shock-bang time, it only causes an arrival time spread of ~ 30 ps at the PTD. To correct for the arrival time spread caused by T_i and its evolution, 1D calculations of the $T_i(t)$, using the hydrocode LILAC,[24] were used in the analysis. T_i was determined from the ratio of DD and D^3He reaction rate for conditions of equal molar D and ^3He, and under the assumption of a uniform density and temperature profiles.

The geometric broadening starts to be more significant as the capsule compresses, and at compression-bang time its contribution to the arrival time spread at the PTD is about 30 ps. The geometric broadening is caused by the finite size and shape of the proton source and shell. Even in a spherical capsule implosion, protons transverse the compressed shell at different angles to the shell normal and thus travel different path lengths through the shell. This results in a range of energy downshifts, which in turn corresponds to an arrival time spread at the PTD. To quantify and correct for this effect, 3D Monte Carlo calculations were used to distribute birth location of each proton and its path length in the fuel and shell, which gives the amount of energy lost and thus the arrival time at the PTD. Proton core imaging spectroscopy (PCIS) (Ref. 25) provided information about the size and shape of the proton source at compression-bang time, and a Gaussian source radius ($1/e$) of about ~ 35 μm was used. Additional information about the source size was obtained from other work,[11,12] which demonstrated that the convergence ratio[26] is a factor 2 smaller at shock-bang than at compression-bang time, indicating a source radius of ~ 70 μm at shock-bang time. The evolution of the source size through the D^3He burn was estimated from a linear interpolation between these two times.

The time evolution of ρR is the third component causing arrival time spread at the PTD. As the capsule compresses, ρR and proton energy downshift increase. During the entire D^3He burn, the proton energy downshift typically varies from 0.5 MeV (at shock-bang time) to 3.5 MeV (at maximum compression), corresponding to an arrival time spread of about ~ 200 ps, which broadens the real burn history by $\sim 40\%$. It is therefore important to determine $\rho R(t)$ and its

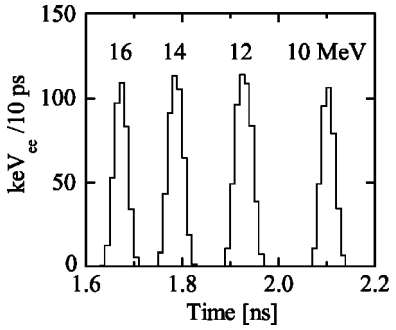

FIG. 3. Determined arrival times at the PTD for protons with energies ranging from 10 to 16 MeV. A time dispersion of ~70 ps/MeV is introduced by positioning the PTD 9 cm from the implosion. The PTD light response to protons, which is given in keV_{ee}/10 ps (subscript *ee* stands for electron equivalent), is also indicated. Accounting for the 20 ps risetime (caused by scintillator and streak camera response) and excluding the effect of the long scintillator decay time, the total scintillator response is determined to be ~40 ps (FWHM).

effect on the measured PTD data. Figure 3 shows the arrival time for protons with energies ranging from 10 to 16 MeV. Also shown in Fig. 3 is the proton interaction time, which will be addressed in the next paragraph.

The last component causing time spread is the PTD response. Since the burn history is encoded in the leading edge of the measured PTD signal, streak camera response and scintillator risetime ~20 ps needs to be corrected for as well as the proton interaction time with the scintillator. These effects have been accounted for in the analysis, and the PTD light response to protons with energies varying from 10 to 16 MeV is shown in Fig. 3 for a 1.0 mm thick BC422 scintillator. It is seen in Fig. 3 that the 1 mm scintillator response is ~40 ps (FWHM) irrespective of proton energy.

B. Determination of $\rho R(t)$ and D^3He burn history

$\rho R(t)$ was determined by fitting a calculated, time integrated proton spectrum to a measured spectrum (a set of measured spectra is shown in Fig. 1). The best fit was found by minimizing χ^2 between measured and calculated spectra by varying the fitting parameters in the function used for $\rho R(t)$. Three different types of $\rho R(t)$ functions were tried (Lorentzian, a skewed Gaussian, and a higher-degree polynomial), and they gave the same results within the uncertainties. The calculated, time integrated spectrum was constructed as follows. At a particular time t the birth spectrum of the D^3He protons broadens due to ion temperature and implosion geometry, and is downshifted in energy due to ρR. Provided that the proton production history (or D^3He burn history) is known, a time integrated D^3He proton spectrum can be determined by summing all proton spectra, each produced at a particular time t, over the entire D^3He burn. However, since the real proton production history is not known at this point, the DD neutron production history was initially used in the analysis in a fashion similar to the method described Ref. 16. The NTD measured DD neutron production history (which is not sensitive to the shock) could be satisfactorily used in this analysis if the shock yield is insignificantly small, or if the shock component in the D^3He proton energy spectrum is excluded.

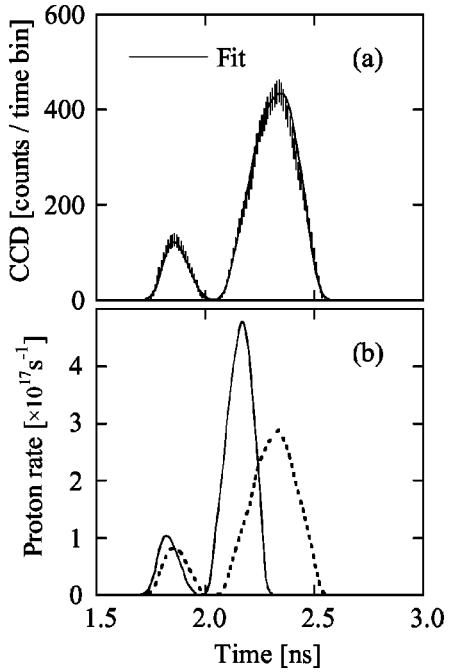

FIG. 4. (a) Calculated D^3He burn history (solid line) fitted to deconvolved PTD signal, which is indicated by the error bars, for a 27 μm thick capsule implosion (shot 31271). (b) Unfolded D^3He burn history compared to the deconvolved PTD signal for the same shot. The effects of the dispersion mechanisms and the initial assumption that all protons have energy of 14.3 MeV are illustrated by comparing the differences of the two time histories. The deconvolved PTD signal has been normalized to the unfolded D^3He burn history to allow for a detailed comparison of the shape of the two time histories.

Having quantified the effects causing time dispersion at the PTD, the D^3He burn history can be inferred from the deconvolved PTD signal shown in Fig. 2(c). A semianalytical forward-fitting technique was used in which a guessed D^3He burn history was folded with the components causing the arrival time spread at the PTD [an average $\rho R(t)$ was used in this part of the analysis]. Two skewed super Gaussians, representing the shock peak and compression peak, were used as an initial guess of the real D^3He burn history and folded with the components causing time dispersion. The convolution was adjusted to the deconvolved PTD signal (shot 31271), using a χ^2 minimization technique, and the best fit is shown in Fig. 4(a). The effects of the dispersion mechanisms and the initial assumption that all protons have an energy of 14.3 MeV are illustrated in Fig. 4(b) in which unfolded D^3He burn history is compared to deconvolved PTD signal. The unfolded D^3He burn history can now be used to infer the final $\rho R(t)$ curves by fitting calculated, time integrated proton spectra to measured spectra. An example of a resulting set of calculated D^3He proton spectra that have been fitted to the measured spectra (including a significant shock component) is shown in Fig. 5(a) for shot 31271. The inferred $\rho R(t)$ curves from these fits, and the unfolded D^3He burn history (dotted line) are shown in Fig. 5(b).

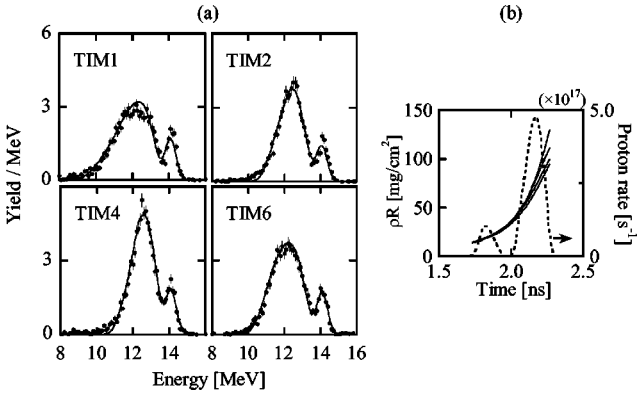

FIG. 5. (a) Calculated D^3He proton spectra, for a 27 μm thick capsule implosion (shot 31271), fitted to spectra measured by proton spectrometers positioned in TIM1 through TIM6 (a reduced χ^2 ranging from 0.7 to 1.0 were obtained from these fits). (b) Unfolded D^3He burn history (dotted line), and final $\rho R(t)$ curves inferred from the fits shown in (a).

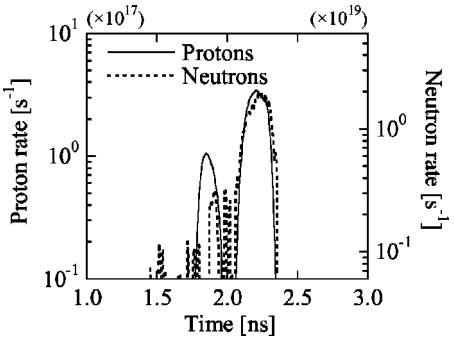

FIG. 6. D^3He and DD burn histories for a 27 μm thick capsule implosion (shot 31274). The D^3He burn history contains a significant shock-burn component in addition to a compression burn, similar to that of DD neutrons. In this particular case the total DD yield is ~60 times larger than the D^3He yield.

IV. RESULTS

A. Nature of the D^3He burn history

The D^3He burn history strongly depends upon the type of capsule imploded and the shape and strength of the laser drive. For these experiments, a strong first shock is generated, which elevates the temperature to ~100 eV when it breaks out at the shell's inner surface. A second, faster shock subsequently breaks out into the shocked fuel, and coalesces with the first shock before it reaches the center of the implosion. As the shock front, driven by the second wave, moves towards the target center, spherical effects further increase its strength and velocity, and at shock convergence a large fraction of the kinetic energy is transformed into thermal energy of the ions. This is the onset of the shock burn. Additional heating is produced by the reflected shock as it expands outwards and thus increases the pressure about an order of magnitude.[27] Consequently the D^3He reaction rate increases for ~100 ps. Eventually as the shock wave expands, it gradually loses strength (due to the spherical geometry) and the fuel starts to cool off, thus reducing the D^3He reaction rate. As a result, the overall shock-burn duration is typically 100 ps (FWHM). As the capsule compresses during the deceleration phase, which most notably begins when the reflected shock impacts the fuel-shell interface, the pressure, density, and temperature increase until conditions are reached again for D^3He fusion to occur. This phase is identified as the compression burn, which occurs a few hundred picoseconds after the shock burn and continues for ~150–200 ps.

As shown in Fig. 6, the D^3He burn history contains a significant shock-burn component in addition to a compression burn, for a 27 μm capsule implosion (shot 31271), that is similar to that of DD neutrons. In this case, the total DD yield is ~60 times larger than the D^3He yield. As indicated in Fig. 6, the unique strength of the D^3He shock burn and its clear separation from the compression burn, as opposed to DD shock burn, allow highly accurate measurements of the shock-bang timing.

As demonstrated, the measured DD and D^3He burn histories contain vast amounts of information about the implosion. Additional information, such as evolution of ion temperature $T_i(t)$, can be determined from the ratio of the DD and D^3He burn histories. Assuming uniform density and temperature profiles, this ratio is strongly dependent on ion temperature allowing an estimate of the average $T_i(t)$.[8] Figures 7(a)–7(c) show the experimentally determined $T_i(t)$'s for 20, 24, and 27 μm thick capsule implosions (black points), respectively. The statistical accuracy in the $T_i(t)$ data for each capsule type was improved by summing the DD and D^3He burn history data over a few consecutive shots. A constant temperature (~2–4 keV for the different types of implosions) is inferred during the compression phase. This observation is consistent with previous work that determined a time averaged ion temperature at compression-bang time.[28] Also shown in Figs. 7(a)–7(c) is the 1D calculation of $T_i(t)$ (solid line), which is determined from the ratio of the two burn histories. A sharp cutoff flux limiter of ~0.07 was used in the 1D calculations for 20 and 24-μm cases, while a sharp cutoff flux limiter[29] of ~0.06 was used for the 27-μm case. As shown in Figs. 7(a)–7(c), the experimental data indicate a significantly higher $T_i(t)$ than predicted for the 20 and 24-μm capsule implosions during the final stages of the compression burn, which suggests that mix is significant in these types of implosions. The 27-μm capsule implosion indicates a smaller discrepancy suggesting that mix is less significant in this case.

B. Shock-bang timing and shock-burn duration

The unique strength of the D^3He shock burn and its clear separation from the compression burn allow highly accurate shock-bang timing measurements, and thus highly accurate studies of drive efficiency often characterized by the flux limiter. The advantage of this approach is that mix is insignificant at shock-bang time, as demonstrated in Ref. 12, allowing accurate comparisons of experimental data and 1D calculations. Figures 8(a) and 8(b) contrast the measured shock-bang time and shock-burn duration, respectively, to 1D calculations in which different flux limiters were used. With the assumption that the laser absorption is correctly computed, a flux limiter of ~0.08 and ~0.07 is required to explain the measured shock-bang time for the 20 and 24 μm

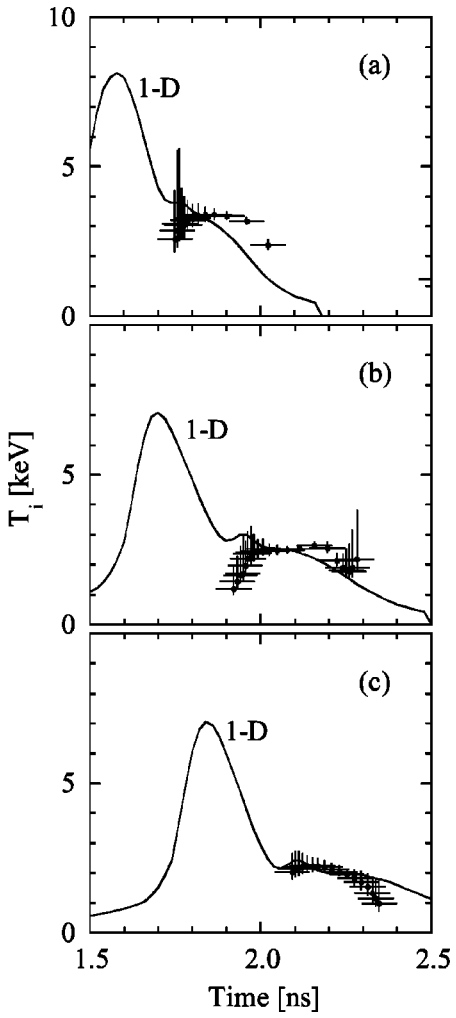

FIG. 7. $T_i(t)$ determined from the ratio of measured DD and D^3He burn histories for 20 μm (a), 24 μm (b), and 27 μm thick capsule implosions (c). The statistical accuracy in the $T_i(t)$ data was improved by summing the DD and D^3He burn history data over a few consecutive shots. For the 20 μm case, the $T_i(t)$ data is averaged over two shots (shots 29835 and 29836), while the $T_i(t)$ data for the thicker capsule implosions is averaged over four shots (29838–29841 for the 24 μm case, and 31271, 31274–31276 for the 27 μm case). A constant temperature of $\sim 2-4$ keV is determined during the compression phase (for the different types of implosions). The measurements are compared to 1D calculated $T_i(t)$ determined from the ratio of the burn histories (solid lines). A sharp cutoff flux limiter of ~ 0.07 was used in the 1D calculations for the 20 and the 24 μm case, while a sharp cutoff flux limiter of ~ 0.06 was used for the 27 μm case. The experimental data indicate a higher $T_i(t)$ than predicted during the final stages of the compression phase for the 20 and 24-μm capsule implosions, which suggests that mix is significant in these types of implosions. The 27-μm capsule implosion indicates a much smaller discrepancy suggesting that mix is less significant in this case.

thick capsule implosions, respectively, while a flux limiter closer to ~ 0.06 must be used to describe the 27 μm data. In addition, the measured shock-burn duration cannot be accurately explained by the 1D calculations that seem to systematically overestimate the shock-burn duration.

C. Evolution of ρR and ρR asymmetry

The D^3He burn history, in combination with several time integrated D^3He proton spectra, provides a method for studying the evolution of ρR and ρR asymmetries, as described in Sec. III. The time integrated spectra are recorded from different views of the implosion, allowing for low mode ($l \leq 3$) ρR asymmetries to be determined.[9] The evolution of ρR and ρR asymmetries, inferred from spectral and temporal measurements, for a 24 μm thick capsule imploded under nominally ideal conditions (shot 29841), is plotted in Fig. 9 for different views (dotted lines), along with a 1D calculation (thin solid line). In addition, Fig. 9 shows the D^3He burn history for this implosion (thick solid line). As indicated, the 1D calculation agrees with the experimental data at shock-

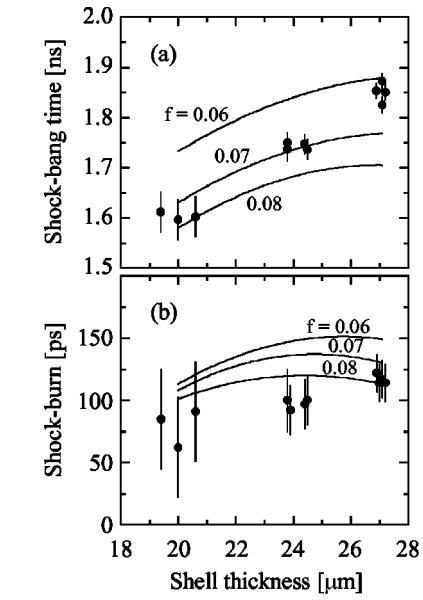

FIG. 8. Measured shock-bang time (a), and measured shock-burn duration (b), as functions of shell thickness. The measurements are contrasted to 1D calculations in which sharp cutoff flux limiters ranging from 0.06 to 0.08 were used. As mix is insignificant during shock burn, accurate comparisons of measured data and 1D calculations can be performed. A flux limiter of ~ 0.08 and ~ 0.07 is required to explain the shock-time data for the 20 and 24 μm thick capsule implosions, respectively, while a flux limiter closer to ~ 0.06 must be used to describe the 27 μm data. Furthermore, measured shock burn duration cannot be accurately explained by the 1D calculations, which seem to systematically overestimate the shock-burn duration.

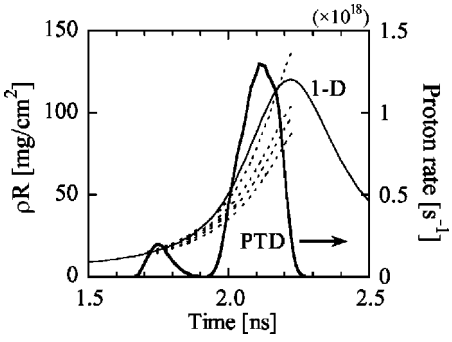

FIG. 9. Evolution of ρR and ρR asymmetries (dotted lines) inferred from experiments for a 24 μm thick capsule imploded under nominally ideal conditions (shot 29841). Also shown is the 1D calculation (thin solid line), which agrees with the experimental data at shock-bang time, but at compression-bang time it overestimates the average ρR with ($\sim 20\%$). An average ρR growth of $\sim 4-5$ times from shock-bang time to compression-bang time is observed. The D^3He burn history is shown as well (thick solid line).

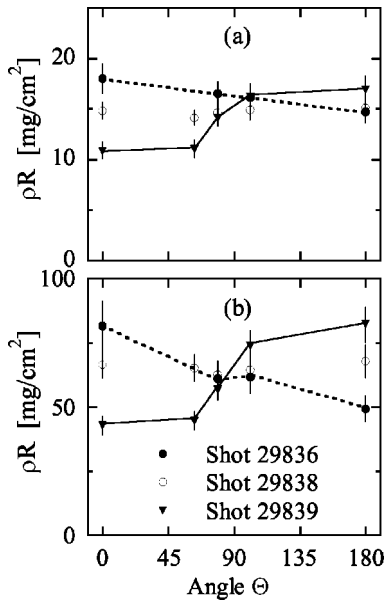

FIG. 10. (a) Measured ρR as a function of longitudinal angle at shock-bang time, (b) and compression-bang time for shots 29836, 29838, and 29839. The overall form of the data, both at shock-bang time and compression-bang time, from shots 29836 and 29839 indicate a dominant structure of mode $l=1$ in longitudinal angle, although there are not enough measurements to rule out the possibility of higher modes. It is also seen that the ρR asymmetries are clearly amplified throughout the implosion without any phase changes. A ρR growth of $\sim 4-5$ times (from shock-bang time to compression-bang time) is observed, while ρR asymmetries grow $\sim 7-10$ times during this time period. The solid and the dashed line are linear interpolations between the points. For comparison, ρR data for a third implosion (shot 29838) is also shown in which no significant low-mode ρR asymmetries are observed.

bang time as also observed in Ref. 16, but at compression-bang time it overestimates the average ρR by $\sim 20\%$, which is larger than the error in the inferred average $\rho R(t)$ (the error is typically 5%–10%). The average ρR grows by a factor of $\sim 4-5$ times from shock-bang time to compression-bang time, and a similar trend is observed for the other types of implosions. Furthermore, ρR asymmetries are also observed at shock-bang time for nominally symmetric implosions, and these asymmetries seem to amplify throughout the implosion without any phase changes. A similar conclusion was suggested in Ref. 13, which compared ρR asymmetries observed at compression-bang time and shock-bang time, an effect that was demonstrated later in Ref. 14 for capsules imploded using a large imposed laser-drive asymmetry. The measured ρR is plotted in Figs. 10(a) and 10(b) as a function of longitudinal angle (although the TIM ports are not all on the equator) for shots 29836 (20 μm thick capsule), 29838, and 29839 (both 24 μm thick capsules) at shock-bang time and compression-bang time. The overall form of the data, both at shock-bang time and compression-bang time, from shots 29836 and 29839 indicate that the dominant structure has a mode number of $l=1$ in longitudinal angle, although there are not enough measurements to rule out the possibility of higher modes. Both Figs. 10(a) and 10(b) also clearly demonstrate that the $l=1$ ρR asymmetry grows $\sim 7-10$ times (from shock-bang time to compression-bang time) without any phase changes. As described in Refs. 14 and 30 the growth of the absolute magnitude of these low-mode ρR asymmetries, which mainly result from laser drive asymmetry (variation in on-target laser intensity), is primarily driven by Bell–Plesset related convergence effects,[31] and the expression for the ρR asymmetry growth can be derived from Eq. (3) in Ref. 30 and expressed as

$$\frac{\Delta\rho R(t)}{\Delta\rho R_s}=\frac{[Cr(t)-1]}{[Cr_s-1]}\frac{\langle\rho R(t)\rangle}{\langle\rho R\rangle_s}. \tag{3}$$

Here $\Delta\rho R(t)$ is the evolution of ρR asymmetry, $\Delta\rho R_s$ is the ρR asymmetry at shock-bang time, $Cr(t)$ is the time dependent convergence ratio as defined in Ref. 26, $\langle\rho R(t)\rangle$ is the evolution of the average ρR, Cr_s and $\langle\rho R\rangle_s$ are the convergence ratio and average ρR, respectively, at shock-bang time. Using the definition of $Cr(t)$ it can be shown that the convergence ratio is ~ 10 for these types of implosions at compression-bang time, which is about a factor 2 larger than at shock-bang time. With this information in hand, Eq. (1) can be written as

$$\frac{\Delta\rho R(t)}{\Delta\rho R_s}\sim 2\frac{\langle\rho R(t)\rangle}{\langle\rho R\rangle_s}, \tag{4}$$

indicating that $\Delta\rho R$ should grow ~ 2 times as fast as the $\langle\rho R\rangle$. This is also observed in these experiments, as shown in Figs. 10(a) and 10(b), which illustrates that the $\Delta\rho R$ grows about a factor of 2 faster than the $\langle\rho R\rangle$ for shots 29836 and 29839. For comparison, ρR data for a third implosion (shot 29838) is also shown in Figs. 10(a) and 10(b), and for this particular implosion no significant ρR asymmetries are observed, both at shock-bang time and compression-bang time.

V. FUTURE WORK

Several intriguing avenues exist for advancing this work. First, we will study the evolution of ion temperature at earlier times (during the shock phase) using the method described herein. We have also initiated similar studies of the time evolution of fuel-shell mix in ^{3}He filled CD capsule implosions. In principle, studies of ^{3}He seeded cryogenic D_2 implosions at OMEGA that utilize these types of measurements could extend experimental information about the dynamics of cryogenic implosions. This type of data would significantly improve our understanding of how assembly occurs and allow critical evaluations of numerical simulations. It also seems plausible that similar measurements could be performed at the NIF at various phases in the development and testing of preignition capsules. In addition, with the capability of the PTD to time separate 14.1 MeV neutrons from ~ 20 to 30 MeV tertiary protons,[32] ρR evolution and asymmetries might be discernable for a large class of implosions that use D–T–^{3}He fills.

VI. CONCLUSIONS

Shock-bang timing and proper assembly of capsule mass, as manifested through ρR evolution, have been determined for D^{3}He capsule implosions. The primary goal of these experiments was to improve and extend the experimen-

tal information of the capsule implosions dynamics. Utilizing simultaneously the proton temporal diagnostic (PTD), the neutron temporal diagnostic (NTD), and several proton spectrometers, accurate studies of the nature of the D^3He and the DD burn were determined. In particular, studies of shock-bang timing, evolution of ion temperature, evolution of ρR and ρR asymmetries were performed. These studies demonstrate accurate comparisons, hitherto unavailable, between measurements and numerical calculations at shock-bang time. Comparisons of measured $T_i(t)$ to 1D calculations seem to indicate that the measured T_i is higher than predicted in the later stage of the compression phase illustrating the effect of mix during this period. Finally, it has been shown that ρR asymmetries exist at shock-bang time for nominally symmetric implosions, and that these asymmetries ($l=1$) are amplified throughout the implosion without any phase changes. It has also been shown that ρR asymmetries grow ~ 2 times as fast as the average ρR growth.

ACKNOWLEDGMENTS

The authors express their gratitude to the OMEGA engineers and operations crew who supported these experiments.

This work has been supported in part by LLE (Subcontract No. P0410025G) and LLNL (Subcontract No. B313975), and by the U.S. Department of Energy Office of Inertial Confinement Fusion (Grant No. DE-FG03-99DP00300) and under Cooperative Agreement No. DE-FC03-92SF19460, the University of Rochester, and New York State Energy Research and Development Authority.

[1] S. W. Haan, S. Pollaine, J. D. Lindl *et al.*, Phys. Plasmas **2**, 2480 (1995).
[2] J. D. Lindl, R. L. McCrory, E. M. Campbell *et al.*, Phys. Today **45**(9), 32 (1992).
[3] J. D. Lindl, Phys. Plasmas **2**, 3933 (1995).
[4] M. D. Rosen, Phys. Plasmas **3**, 1803 (1996).
[5] M. Andre, M. Novaro, and D. Schirmann, Rev. Sci. Tech. Direction Appl. Militaires **13**, 73 (1995); J. Maddox, Nature (London) **372**, 127 (1994).
[6] T. R. Boehly, D. L. Brown, R. S. Craxton *et al.*, Opt. Commun. **133**, 495 (1997).
[7] C. K. Li and R. D. Petrasso, Phys. Rev. Lett. **70**, 3059 (1993).
[8] C. K. Li, D. G. Hicks, F. H. Séguin *et al.*, Phys. Plasmas **7**, 2578 (2000).
[9] F. H. Séguin, J. A. Frenje, C. K. Li *et al.*, Rev. Sci. Instrum. **74**, 975 (2003).
[10] F. H. Séguin, C. K. Li, J. A. Frenje *et al.*, Phys. Plasmas **9**, 2527 (2002).
[11] F. H. Séguin, C. K. Li, J. A. Frenje *et al.*, Phys. Plasmas **9**, 3558 (2002).
[12] R. D. Petrasso, J. A Frenje, C. K. Li *et al.*, Phys. Rev. Lett. **90**, 095002 (2003).
[13] F. H. Séguin, C. K. Li, J. A. Frenje *et al.*, Bull. Am. Phys. Soc. **47** (2002).
[14] F. H. Séguin, J. R. Rygg, J. A. Frenje *et al.*, Bull. Am. Phys. Soc. **48**, 57 (2003).
[15] C. K. Li, F. H. Séguin, J. A. Frenje *et al.*, Phys. Plasmas **10**, 1919 (2003).
[16] V. A. Smalyuk, P. B. Radha, J. A. Delettrez *et al.*, Phys. Rev. Lett. **90**, 135002 (2003).
[17] Y. Lin, T. J. Kessler, and G. N. Lawrence, Opt. Lett. **20**, 764 (1995).
[18] S. Skupsky, R. W. Short, T. Kessler *et al.*, J. Appl. Phys. **66**, 3456 (1989).
[19] T. R. Boehly, V. A. Smalyuk, D. D. Meyerhofer *et al.*, J. Appl. Phys. **85**, 3444 (1999).
[20] V. Yu Glebov, C. Stoeckl, S. Roberts *et al.*, "Proton temporal diagnostic for ICF experiments on OMEGA," Rev. Sci. Instrum. (to be submitted).
[21] R. A. Lerche, D. W. Phillon, and G. L. Tietbohl, Rev. Sci. Instrum. **66**, 933 (1995).
[22] C. Stoeckl, V. Yu Glebov, S. Roberts *et al.*, Rev. Sci. Instrum. **74**, 1713 (2003).
[23] R. A. Lerche and R. L. Griffith, Proc. SPIE **832**, 266 (1987).
[24] J. Delettrez, R. Epstein, M. C. Richardson *et al.*, Phys. Rev. A **36**, 3926 (1987).
[25] J. DeCiantes, B. E. Schwartz, J. A. Frenje *et al.*, Bull. Am. Phys. Soc. **48**, 58 (2003).
[26] The time dependent convergence ratio $[Cr(t)]$ of an implosion is defined as $Cr(t)=\sqrt{[\langle \rho R(t)\rangle/(f\times\rho_0 R_0)]}$, where $\langle \rho R(t)\rangle$ is the evolution of average areal-density, f is the fraction of initial shell not ablated away ($f\sim 50\%$ for a 20 μm capsule implosion), and $\rho_0 R_0$ is the initial areal density.
[27] G. I. Guderley, Luftfahrtforschung **19**, 3032 (1942).
[28] J. Delettrez, Can. J. Phys. **64**, 932 (1986).
[29] P. B. Radha, J. Delettrez, R. Epstein *et al.*, Phys. Plasmas **9**, 2208 (2002).
[30] C. K. Li, F. H. Séguin, J. A. Frenje *et al.*, Phys. Rev. Lett. (submitted).
[31] M. S. Plesset, J. Appl. Phys. **25**, 96 (1954).
[32] R. D. Petrasso, C. K. Li, M. D. Cable *et al.*, Phys. Rev. Lett. **77**, 2718 (1996).